ORIGINAL ARTICLE

Effect of ball size and impact velocity on the microstructure and hardness of surface mechanical attrition–treated 304L steel: experiment and finite element simulations

Vikesh Kumar[1] · Anurag Sharma[2] · Santosh Sattappa Hosmani[1] · Indrasen Singh[2]

Abstract

In surface mechanical attrition treatment (SMAT), the processing parameters like the diameter of hardened steel balls/shots (D) and their impact velocity (V) are crucial in affecting the mechanical properties of the materials. This study is focused on understanding the effect of D and V on microstructural and hardness variation during the SMAT process. The SMAT has been performed on AISI 304L steel using 3-mm and 8-mm diameter balls with a combination of 1 m/s and 10 m/s impact velocity. Microstructure of the SMATed material shows twin distribution near the top surface changeover from coarser to finer when V increases from a low to significantly high value, whereas it changes marginally with an increase in D. Nanoindentation experiments performed along the depth of SMATed material reveal that the near-surface hardness is mainly governed by V and weakly influenced by D. However, the hardened layer thickness is enhanced by increasing either of these parameters. The complementary finite element (FE) simulations of the single impact SMAT process are performed using the rate-dependent Johnson–Cook plasticity model to provide the mechanistic reasons for the behavior observed from the experiments. A strategy to determine the hardness-depth profile of SMATed steel through FE simulations is developed. The hardness behavior of the SMATed steel is linked to the effects of D and V on the residual equivalent stress and equivalent plastic strain at the surface. The hardness away from the surface is influenced by the shot size and shot velocity. The empirical relations that show the dependence of hardness on the SMAT parameters are determined.

Keywords SMAT · AISI 304L stainless steel · Nanoindentation · Hardness · Finite element analysis

1 Introduction

Stainless steels have wide applications in various industries owing to their excellent mechanical properties such as high-yield strength, ductility, and corrosion resistance [1–4]. Notwithstanding these attractive properties, in many applications, the engineering components made of stainless steel fail due to crack initiation caused by the inferior surface properties (e.g., lower surface hardness) [5–7]. Such behavior has encouraged researchers to develop various techniques to improve surface properties. Among these, severe plastic deformation (SPD) techniques including cold rolling [1], shot peening (SP) [8], surface mechanical attrition treatment (SMAT) [9–11], and laser shock peening [12] are the most promising approaches. These techniques improve the surface properties such as hardness, strength, wear resistance, and fatigue resistance through nano-crystallization, resulting in gradient in microstructure near the surface [10–13].

In the conventional shot peening process, spherical- or irregular-shaped particles with an average diameter ranging from 0.25 to 1 mm are impacted on the specimen surface with a velocity of around 20–150 m/s [11]. The SMAT process, introduced first time by Ke and Jian in 1999 [9], improves the surface mechanical properties via severe deformation caused by the impact of randomly moving balls/shots of hardened steel or ceramics (Fig. 1). The SMAT process looks similar to the shot peening, but it is significantly different from the latter in various aspects. For instance, the diameter of the balls used in the SMAT process ranges from

✉ Indrasen Singh
  indrasen@iiti.ac.in

1 Department of Metallurgy Engineering and Materials Science, Indian Institute of Technology Indore, Simrol, Indore 453552, India

2 Department of Mechanical Engineering, Indian Institute of Technology Indore, Simrol, Indore 453552, India
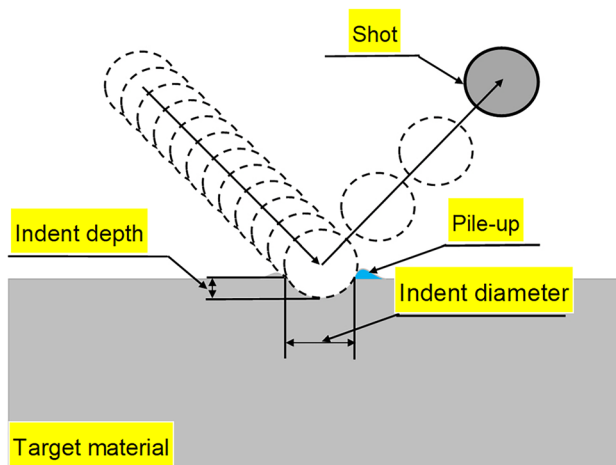
Fig. 1 Schematic diagram showing the impact of a shot on the target with a certain velocity and a specified angle

1 to 10 mm, which is much larger than the conventional shot peening [10, 11]. Impact velocities in SMAT are significantly lower (varies from 1 to 20 m/s [14]) than the traditional shot peening. SMAT usually generates a gradient structure to a considerably higher depth in the treated material than shot peening [15, 16]. Consequently, SMAT can enhance the ballistic performance of steels significantly due to reduced deformation in the direction of impact [17]. The SMAT is found to be suitable for various applications such as aerospace (e.g., high/low-pressure blades and impellers), automotive (e.g., camshaft and compressor wheel), infrastructure (e.g., welded structures), and medical (e.g., surgical instruments and implants) [18–20].

The diameter of the shots/balls, D, and the impact velocity, V, are the key parameters influencing the plastic deformation; and hence, mechanical properties of the treated surface through SMAT process. Indeed, Chan et al. [21] reported that the strain rate developed in the material during the SMAT process is proportional to V. It must be noted that higher strain rate can generate the nanostructures more efficiently, leading to more desirable properties in materials. SMAT results in strain rate of the order of 10^3–10^5 s^{-1} and accumulation of considerable plastic strain on the treated surfaces [22, 23]. Consequently, a pronounced dislocations' activity, formation of deformation-induced twins, and deformation-induced phase-transformation take place in the treated layer [24]. Arifvianto et al. [25] investigated the effect of ball size, treatment duration, number of balls, and motor rpm on the microhardness of treated surface of AISI 316L steel and showed that surface hardness increases with increase in D. However, they have not studied the effects of these parameters on microstructural changes of AISI 316L. Gatey et al. [10] have analyzed the effect of D on the variation of microhardness and microstructure along the treated

layer in AISI 304L steel, but the effect of shot velocity was not studied in detail in this work. Samih et al. [26] analyzed the effect of the amplitude of vibration of the sonotrode and treatment duration on the distribution of the geometrical necessary dislocations (GND) density and grain size in the treated layer of AISI 316L steel. In addition to these parameters, the effect of the cryogenic temperature (during SMAT operation) on the hardness and volume fraction of martensite (α') in AISI 304L steel was also investigated by Novelli et al. [27]. It must be noted that the effect of specific velocity of impacting balls on the mechanical properties and microstructure of treated material requires more study. The effect of V was analyzed by varying the sonatrode amplitude or motor rpm in the literature [25–27]. However, conversion of such parameters into velocity (expressed in m/s) is not easily available in most of the literature. As the velocity of balls affects the percentage coverage, the direct correlation/effect of specific velocity on microstructure and properties (keeping a constant peening intensity) would be useful to widen the scope of SMAT technology.

Edberg et al. [28] performed FE simulations of a single impact on elastoplastic and visco-plastic materials and reported a similar trend in residual stress in both materials. Guagliano [29] found that the layer's thickness (with compressive stress) increases marginally with increase in V, while it enhances considerably with D. They also noticed that the maximum value of compressive residual stress increases marginally with enhancement in either V or D. Astaraee et al. [14] estimated the surface coverage during the SMAT processing of pure aluminum through experiments and complementary FE simulations. Their FE predictions on surface coverage, residual stresses, and thickness of the treated layer were in line with the experimental data. Chen et al. [30] investigated the effect of impact velocity on the twin volume fraction, dislocation density, and martensitic transformation near the top surface through numerical simulations of a single impact SMAT by employing a dislocation-density–based model. It must be noted that the primary focus of these studies was to understand the development of the plasticity and residual stresses in the SMATed materials.

Thus, which parameter (among D and V) would affect hardness more predominantly is not clear from above studies. In other words, it is not clear what would be the optimum values of D and V to achieve desired hardness in the treated material. The following issues need to be addressed to choose a suitable combination of process parameters to achieve desired mechanical properties through SMAT: (i) Does the twin density near the treated surface depend on both or either of the parameters, D and V? (ii) How do the parameters D and V influence equivalent plastic strain and stresses in a teated material? (iii) Do the parameters D and V influence hardness near the surface and inside the treated layer in a similar manner? (iv) What is the functional relationship between the hardness

and the parameters D and V? (v) What is the effect of the parameters D and V on the thickness of the hardened layer?

As mentioned above, the simulation approach is slowly being evolved in the SMAT domain. Current work also focuses on this direction. Such study will help predicting (directly or indirectly) the trend in some properties (in particular hardness), which can be used in industry. Stainless steel is an important class of material concerning its engineering and biomedical applications. In this work, experimental and complementary FE simulations of SMAT processing of AISI 304L steel are performed using the rate-dependent Johnson–Cook Material Model. A new strategy to compute the hardness in SMATed layer using different processing parameters through FE simulations is presented in this study. It must be mentioned that no such FE simulations have been performed to predict the hardness variation along the treated layer in a SMATed material, to the best of the authors' knowledge. The approach proposed in this work can also be applied to predict the mechanical response (such as hardness, tensile, fatigue) of pre-stressed/strained (such as SMAT, rolling, high-pressure torsion (HPT), and equal-channel angular pressing (ECAP) processed) materials through FE simulations. Such simulations would help in minimizing the number of experiments and associated costs to optimize the processing parameters to achieve the desired hardness and its gradient along the treated layer. Experimental results suggest that SMAT behavior of AISI 304L steel is a complex function of SMAT parameters like size and velocity of shots. The FE results shed light on the effect of D and V on the size and shape of the indent. Furthermore, empirical relations are presented using given parameters D and V to predict the size of indent produced during SMAT. Furthermore, the functional dependence of hardness (H) versus depth (Z) profiles on the parameters D and V is presented. The present study provides guidelines in choosing an appropriate combination of process parameters D and V to achieve the desired hardness inside the treated layer of SMATed material.

2 Experimental

2.1 Methodology

Commercial AISI 304L stainless steel (the chemical composition is shown in Table 1) was used for the experiments. Cylindrical specimens of 50-mm diameter and 5-mm thickness were prepared from the as-received AISI 304L steel rod. Specimens were surface treated at room temperature using in-house fabricated mechanical-vibration-type SMAT setups. SMAT was carried out using hardened bearing-steel balls (65

HRC), which were jiggled using a vibrating plate. The velocity of balls in SMAT cabin was measured using a high-speed camera. Frequency and amplitude of vibrating plate for 10 ($\pm$1.2) m/s velocity balls were 300 Hz and 15 mm, respectively. However, for velocity of 1 ($\pm$0.2) m/s, vibrating plate had 100 Hz frequency and 3 mm amplitude. The distance between the vibrating plate and the specimen was ~40 mm. About 25% area of the vibrating plate was covered by balls. These parameters were kept constant for all experiments. Size of the balls was 3 mm (136 balls) and 8 mm (19 balls). The SMAT processing of specimens was performed for 120 min and 10 min for 1 m/s and 10 m/s velocity, respectively, to maintain the same percentage coverage (which is linked to the number of times the projected surface is peened entirely by the attrition balls during the SMAT duration [10]) on the treated surface. Thus, in all SMAT experiments, the 1200% coverage was maintained. All the specimens were polished using SiC papers (up to 1500 grit-size) and then cleaned with acetone before performing SMAT. A cross-section of the SMATed specimens was prepared using the conventional metallography steps, i.e., grinding, polishing, and etching (using 25 mL HCl + 25 mL H_2O + 4 g $CuSO_4$ for 30–40 s). X-ray diffraction (XRD) was carried out on non-SMATed and SMATed samples, where CuK_α radiation ($\lambda = 1.5406$ Å) and 2θ angle in the range of 30°–90° were used to record the XRD patterns. For EBSD experiments, specimen was electro-polished. Electropolishing was performed using Struers Lectropol-5 equipment. An electrolyte of methanol and perchloric in the ratio of 80:20 was used at 273 K and 18 V DC. The EBSD maps were obtained using 20 kV accelerating voltage with 200 nm step-size for non-SMATed specimen and 50 nm step-size of SMATed specimen. The scanning electron microscope (SEM) was used for the microstructural analysis. Nano-hardness across the cross-section of the SMATed specimens was measured using Berkovich indenter (tip radius of ~300 nm) at 8000 µN maximum load with 5 s dwell time, and hardness was calculated using Oliver–Pharr method.

2.2 SMAT processed AISI 304L steel: experimental observations

Figure 2a, b shows the IPF and phase maps of non-treated 304L steel characterized by electron backscatter diffraction (EBSD). IPF map shows randomly oriented equiaxial austenitic grains with the average grain size of ~27 ($\pm$10) µm and the phase map shows the presence of delta-ferrite (δ-Fe) in the microstructure, which generally forms during the solidification of steel. Figures 3 and 4 show the SEM micrographs of the cross-section of AISI 304L stainless steel specimens

Table 1 Chemical composition of the AISI 304L stainless steel used in the current study

Element	C	Cr	Ni	Mn	Mo	Si	P	S	N	Fe
Wt.%	0.037	18.01	7.98	1.84	0.38	0.29	0.03	0.001	0.13	Balance

Fig. 2 Electron backscatter diffraction (EBSD) results. **a** IPF and **b** phase map of non-treated 304L steel. **c** IPF and **d** phase map of SMATed 304L steel. **e** X-ray diffraction (XRD) patterns of non-SMATed and SMATed 304L steel
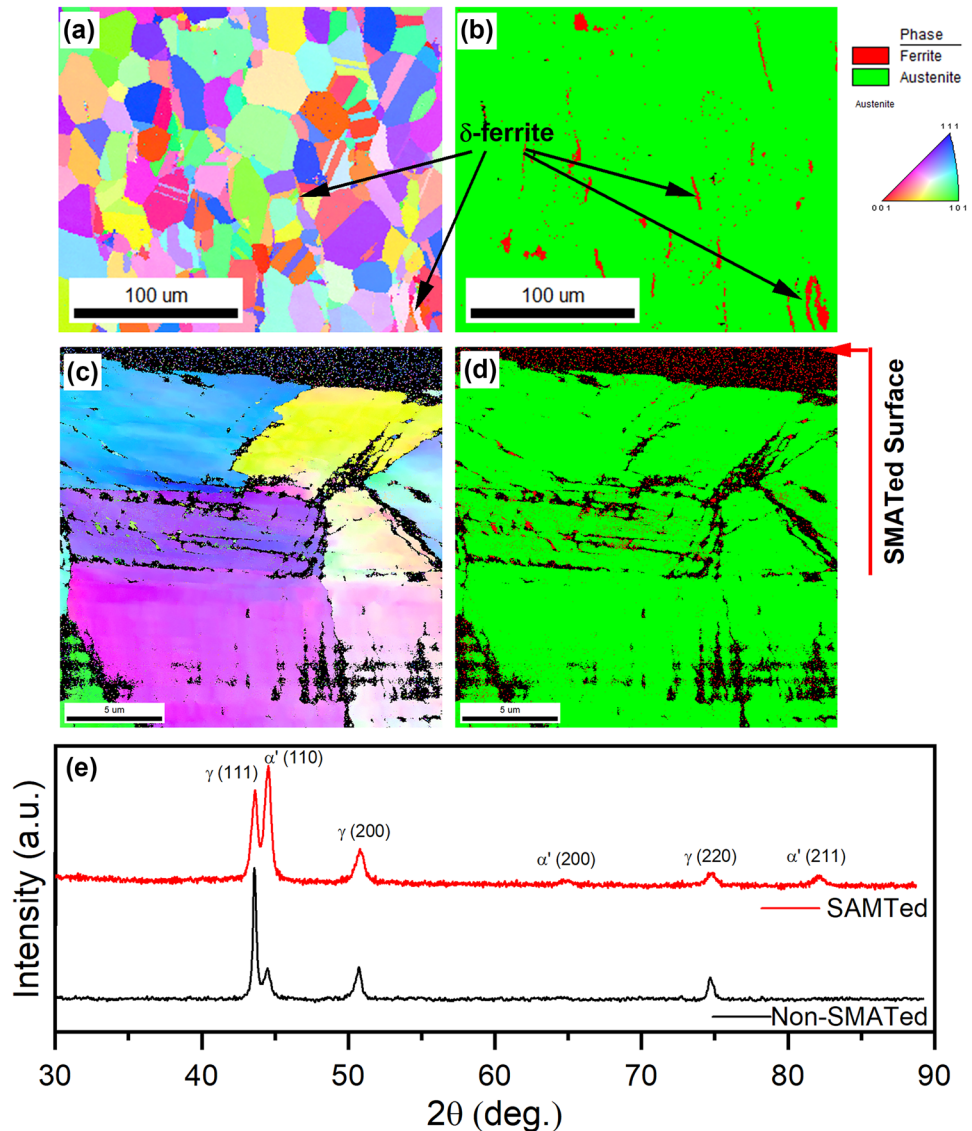

SMATed using 3-mm and 8-mm diameter balls, respectively. The magnified view of the surface regions (Fig. 3a, b) are displayed in Fig. 3c, d. In Figs. 3 and 4, formation of deformation twins can be observed throughout the grains near the surface region of the SMATed specimens, irrespective of ball diameter and impact velocity. This observation is linked to the stacking fault energy (SFE). SFE of AISI 304L steel is about 13 mJ/m², which is considerably lower than the typical threshold level of SFE for twining (18 mJ/m²) to take place [31–34]. Since the influence of colliding balls' impact weakens across the thickness of the specimen, the intensity of deformation twins reduces with an increase in depth. Eventually, it disappears after reaching a certain depth along the cross-section. It is important to note that the thickness of twin-dominated region increases substantially with an increase in the D or V (see Figs. 3 and 4). For instance, in the case of material treated using $V = 1$ m/s, the thickness

of twin-dominated region is increased from ~ 100 μm for $D = 3$ mm to ~ 150 μm for $D = 8$ mm (see Figs. 3a and 4a). However, the enhancement in the thickness with the rise in D is more pronounced for higher impact velocity, as shown in Figs. 3 and 4. The enhancement in impact velocity (while keeping ball diameter fixed) has a similar effect on the thickness of the twin-dominated region, which can be seen by comparing Fig. 3a, b and Fig. 4a, b. It is also important to note that twin spacing is relatively more in Figs. 3c and 4c than that in Figs. 3d and 4d. Thus, the present experiments reveal that *twin distribution near the top surface of SMATed material changeover from coarser to finer when impact velocity increases from a low to significantly high value, irrespective of ball size*.

Furthermore, the presence of coarser twins in both the Figs. 3c and 4c suggests a marginal influence of ball diameter on the intensity of twins near the surface of SMATed

Fig. 3 The SEM micrographs of the cross-section of AISI 304L steel SMATed using 3 mm balls and impact velocity. **a** V = 1 ± 0.2 m/s and **b** V = 10 ± 1.2 m/s. **c** and **d** are the magnified SEM micrographs of the regions shown in a and b, respectively
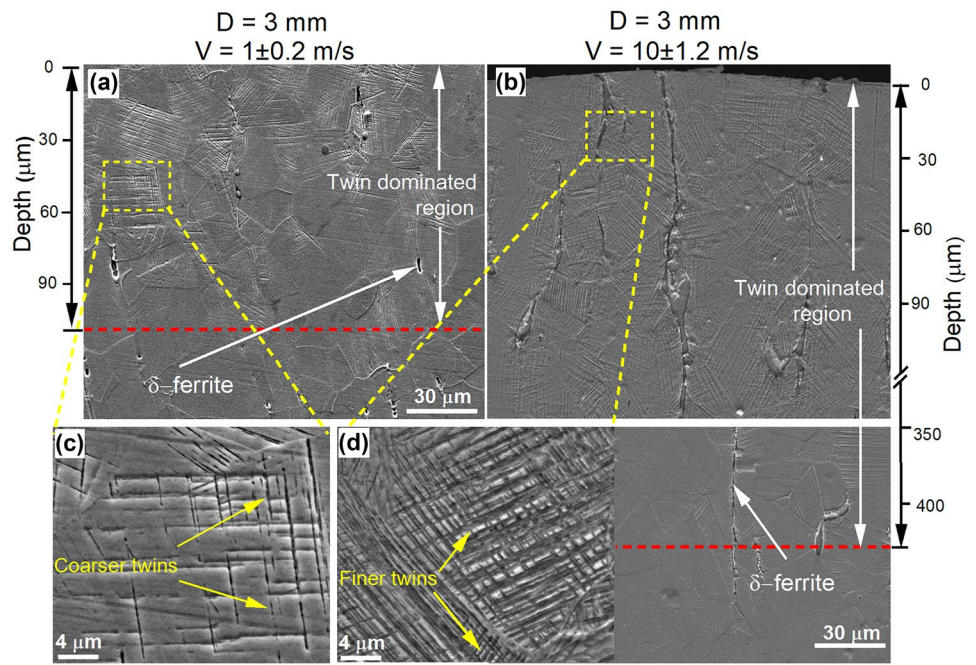

material. In other words, *twin intensity near the surface of SMATed material is mainly governed by impact velocity and marginally influenced by ball diameter.* The finer twins in Figs. 3d and 4d indicate that the material surface treated by higher impact velocity would have experienced more plastic deformation, which would be further confirmed through FE simulations in Sect. 4.

The observed delta-ferrite (δ-Fe) in Figs. 3 and 4 is the part of the as-received microstructure, which can also be seen in Fig. 2b. It must be mentioned that the SMATed

AISI 304L steel has been found to exhibit the formation of deformation-induced martensite (α') owing to low stacking fault energy of the material when subjected to multiple impacts of the vibrating balls [10, 30]. The EBSD results of the near-surface region (Fig. 2c, d) of the SMATed specimen show severe deformation, leading to the unindexed back regions, along with the indexing of some regions as the martensite phase. For the conformation, X-ray diffraction on the non-SMATed and SMATed AISI 304L steel specimens has been performed. The XRD patterns are

Fig. 4 The SEM micrographs of the cross-section of AISI 304L steel SMATed using 8-mm balls and impact velocity. **a** V = 1 ± 0.2 m/s and **b** V = 10 ± 1.2 m/s. **c** and **d** are the magnified SEM micrographs of the regions shown in a and b, respectively
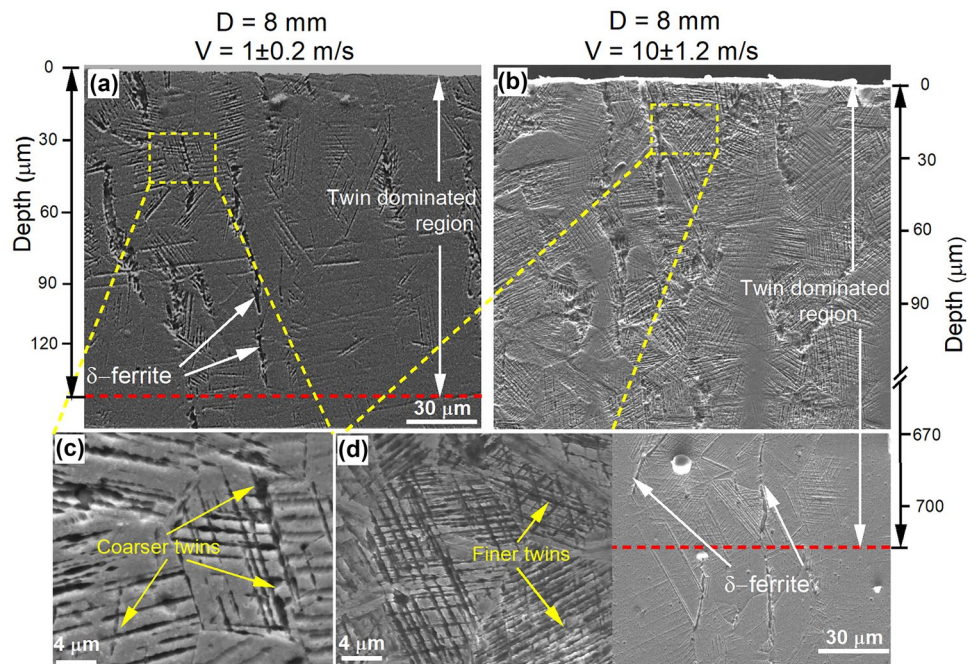
compared in Fig. 2e. The XRD pattern for SMATed sample shows an increase in the intensity of martensite peak (α') in comparison to the non-SMATed steel which confirms the formation of martensite during the SMAT process.

Figure 5a shows a comparison of the indentation load–displacement curves obtained from nanoindentation experiments along the depth of the SMATed specimen and on the surface of the non-SMATed (bare) specimen. This figure shows that the indentation depth in the non-SMATed surface is higher than that in the SMATed surface under the same value of applied load (the maximum load of 8000 μN). Also, the indentation depth after unloading is significantly higher in the former than that in the latter, which confirms higher hardness for SMATed material. Hardness values at different points across the thickness of treated specimens are shown in Figs. 5b, c for fixed values of D and V, respectively, to understand the effect of impact velocity and size

of balls on the hardness profile across the treated layer. It can be seen from Fig. 5b that the hardness of the surface-treated layer using higher impact velocity is more, irrespective of the distance from the surface. The hardened layer's thickness seems to be higher in the material treated using higher impact velocity. In contrast, hardness values near the surface of material treated by two different sizes of balls are almost identical (Fig. 5c), suggesting that *hardness near the SMATed surface is mainly governed by impact velocity; however, it is weakly influenced by the ball diameter.*

Though the present experimental results provide insights on the complex dependence of the mechanical properties of the SMATed austenitic steel on the process parameters (like ball size, and their impact velocity), the following fundamental questions arise at this juncture. Firstly, why are the hardness and twin intensity near the top surface mainly governed by colliding balls' impact velocity? Secondly, what
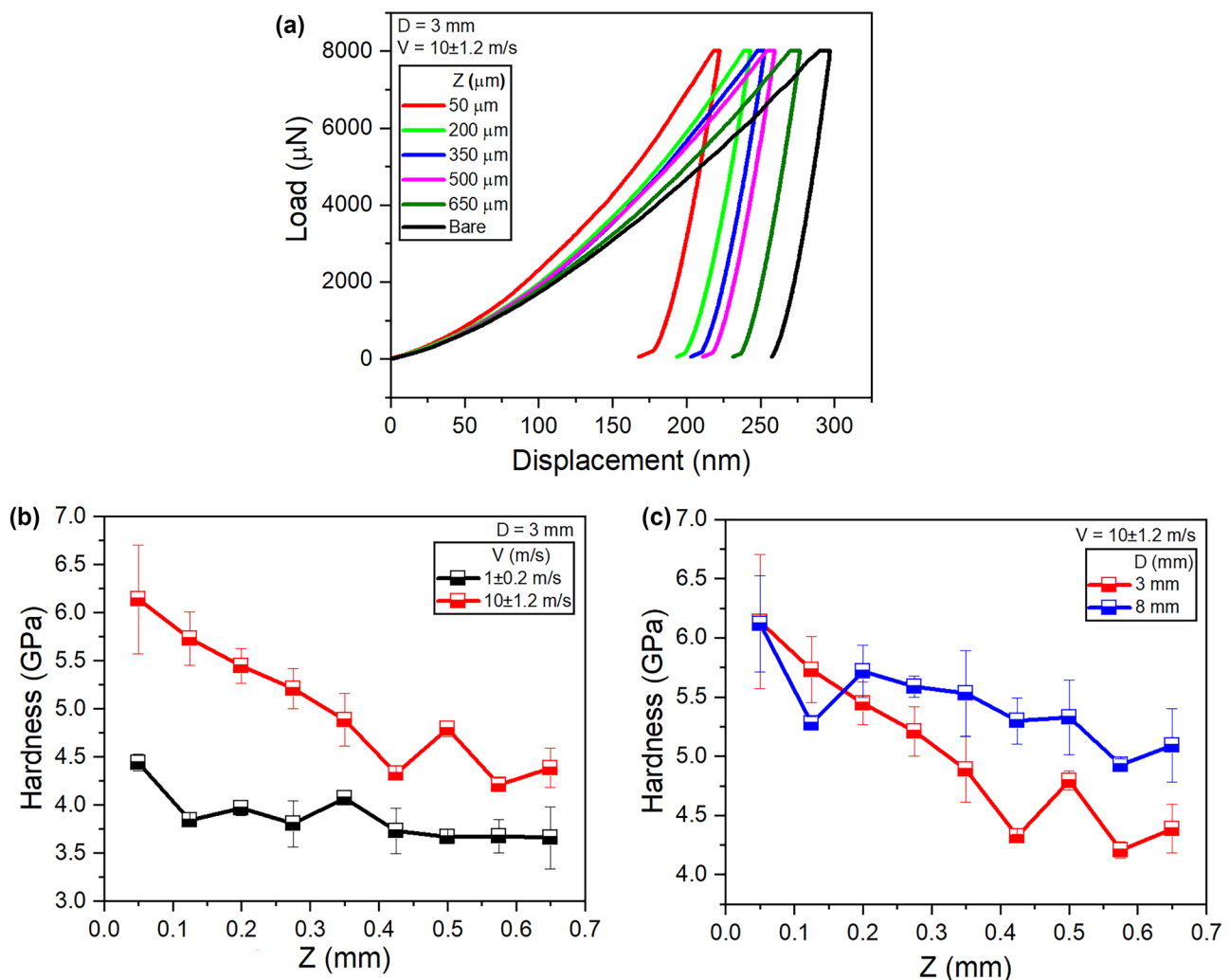
Fig. 5 **a** Comparison of indentation load–displacement curves for SMATed and non-SMATed AISI 304L steel. Hardness values at different points across the cross-section of treated specimens for the fixed values of **b** $D = 3$ mm and **c** $V = 10 \pm 1.2$ m/s

is the best combination of the process parameters to achieve maximum hardness for a given material? Finally, how does the process parameter affect the indent size/shape and treated material's roughness? FE simulations of the single impact of a ball on AISI 304L steel and the computations of indentation along the treated layer are performed in the following sections to address these questions.

3 Finite element simulations of single impact SMAT

3.1 Finite element model

Figure 6a shows a cylindrical target's finite element discretization with an initial size of 20 (L_o) × 20 (H_o) mm using four-node quadrilateral axisymmetric elements with reduced integration (CAX4R) in the $r - z$ plane along with the rigid spherical ball (with diameter D) employed in the simulations of single impact SMAT process. To capture high strain and stress gradient below the indent, a highly refined mesh with the element size of $2.5 \times 10^{-3} L_o$ is used in the target's central region, where the ball is expected to impact; however, a relatively coarser mesh is employed in the outer regions (refer to Fig. 6b). The target's bottom surface is constrained to move along all three directions, while the rigid ball is allowed to move with a prescribed velocity along the z direction. The coefficient of friction between the ball and target material is taken to be 0.2 [35]. To capture the strain rate effects, the plastic flow of the target material is assumed to follow the Johnson–Cook rate-dependent plasticity model [36], which is given as follows:

$$\sigma = \left[A + B\varepsilon^n\right]\left[1 + C\ln\left(\frac{\dot{\varepsilon}}{\dot{\varepsilon}_0}\right)\right]\left[1 - T^{*m}\right], \text{ where } T^* = \frac{T - T_0}{T_m - T_0}. \tag{1}$$

Here, σ and ϵ represent equivalent stress and equivalent plastic strain, respectively. The material constants A, B, and C are initial yield strength (at a reference temperature, T_0 and reference strain rate, $\dot{\varepsilon}_0$), strain hardening coefficient, and strain rate hardening coefficient, respectively. Furthermore, $\dot{\varepsilon}$ and $\dot{\varepsilon}_o$ are applied and reference strain rates, respectively. The parameters n, m, T, and T_m are strain hardening exponent, thermal-softening exponent, current temperature, and melting temperature of the material, respectively. A significant variation in the values of the parameters (appearing in Eq. 1) for AISI 304L stainless steel has been noticed in the literature. For example, the values of the parameters A, B, n, and, C corresponding to reference strain rate, $\dot{\varepsilon}_0$ of $1\ s^{-1}$ are reported to be $253.32 - 310$ MPa, $441 - 1567.33$ MPa, $0.10 - 0.74$, and $0.02 - 0.09$, respectively [37–40]. The parameters A, B, and, n (which characterizes the elastic–plastic response of the material at reference strain rate) are determined by fitting the experimentally obtained nanoindentation P–h curve of non-treated (bare) AISI 304L stainless steel, while the strain rate sensitivity parameter, C, and thermal-softening exponent, m, are taken from Ref. [39]. The values of the material parameters appearing in the plasticity model (refer to Eq. 1) are given in Table 2. Using these material constants, a finite element simulation of Berkovich indentation using Berkovich equivalent spherical-conical indenter is performed. The load–displacement curve predicted by the FE analysis is compared with the experimental data in Fig. 7. It can be seen from this figure that FE predictions are very close to the experimental observations. Computations are performed by considering various values of $D = 3, 5$, and 8 mm, and different values of $V = 1, 5, 10$, and 15 m/s to understand the effect of size and velocity of impacting balls on the distribution of residual stress, strain, and hardness across the SMATed layer of material.

Fig. 6 a Finite element of the model employed in the simulations of a single impact SMAT process. **b** Zoomed-in view of the mesh below the shot
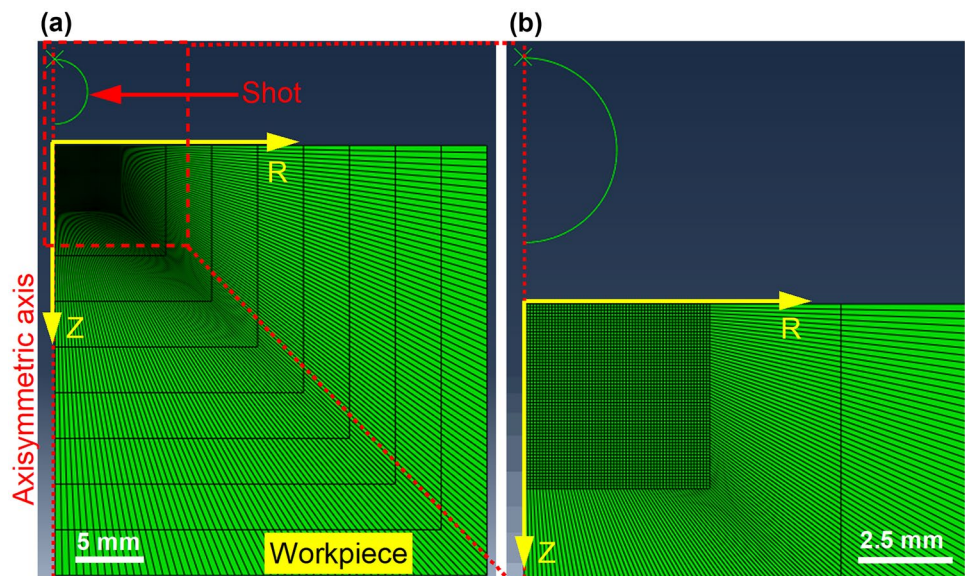
4 Results and discussion

4.1 Effect of D and V on the size and depth of the indent

The size and shape of the impression created due to the impact of a ball on the target material would have a marked effect on the achieved roughness of the SMATed surface. A clear understanding of the influence of processing parameters on the surface roughness of SMATed material is essential to choose an appropriate combination of these parameters to optimize the roughness. Therefore, the influence of the parameters D and V on the indent size and shape is investigated in this section. The contour plots of the displacement, u_z along z direction after the impact of a shot in the $r - z$ plane, are displayed in Fig. 8a. This figure shows that the displacement just below the impression is maximum and decreases rapidly with an increase in depth. The displacement just below the impression is nothing but a permanent plastic deformation, which is generated due to the kinetic energy of ball/shot [27]. Astaraee et al. [14] have also reported a similar surface profile after single impact of a ball through FE simulations. Displacement of a top surface of target SMATed using different sizes of balls with $V = 1$ m/s is plotted against r in Fig. 8b to understand the influence of D on the size and shape of the indent. It can be seen from this figure that irrespective of ball diameter, the magnitude of u_z is maximum at the center of the indent and decreases as one moves away from the center, and eventually, it becomes positive near the periphery of the indent. Finally, u_z becomes zero at far away from the indent, leading to the formation of a hump in the profile of u_z. Such behavior represents a pile-up of material due to plastic flow. Note that the pile-up increases with an increase in D, suggesting an increase in roughness with an increase in ball size. A similar trend can be perceived for a higher velocity of 10 m/s (Fig. 8c). The indent's shape and size are characterized by its diameter, d, and depth, h. In Fig. 8b, the values of d and h for $D = 3$ mm are about 0.24 and 0.046 mm, respectively, suggesting an oblate shaped impression produced by smaller shots. When D is increased to 8 mm, d enhances to 0.52 mm, and h rises to 0.12 mm. Thus, *indent depth rises more rapidly than indent diameter with an increase in ball size*. This behavior, in turn, results in *almost hemispherical indent for bigger balls in contrast to oblate shaped indent for smaller balls*.

Figure 8d, e shows the effect of V on the shape and size of the impression produced by the impact of balls with $D = 3$ and 8 mm, respectively. Note from Fig. 8d that for an impression created using low V of 1 m/s, the values of d and h are around
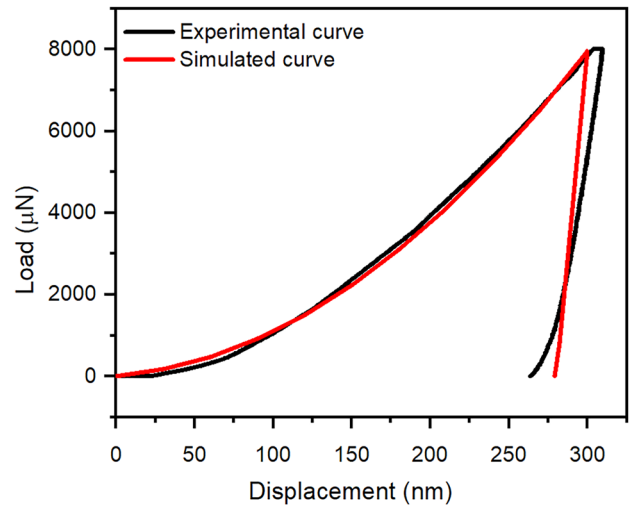
Fig. 7 Comparison between finite element simulation and experimental load–displacement curves from Berkovich indentation

0.24 and 0.046 mm, respectively, which suggest the oblate shape of the impression (as mentioned above). Like the trend observed in Fig. 8b, d and h are increased with an increase in V, while enhancement in the latter is more pronounced than that in the former (Fig. 8d). As a result, the shape of the indent becomes almost hemispherical for higher velocity. A similar trend can also be observed for larger D in Fig. 8e. Thus, it can be concluded from Figs. 8b–d that *an oblate-shaped impression would be created through the impact of a shot having a lower value of either D or V. The shape of the impression would change to hemispherical when either D or V is increased to a significantly large value. Pile-up around the indent increases considerably due to a rise in D or V, which would result in a rougher surface. This observation is in line with the experimental observations mentioned in Ref. [41].*

It would be insightful to plot the variation of h and d against the processing parameters D and V. Therefore, surface plots of h and d in the parametric space of D and V are displayed in Figs. 9a, b, respectively. Note from Fig. 9a that *for a fixed value of ball size, h increases with an increase in V, but the rise in h is more pronounced for bigger balls*. Similarly, h rises marginally with an increase in D for a very low value of V, while it enhances more rapidly when impact velocity is significantly high. A similar trend in d can also be observed in Fig. 9b. Iida [42] has proposed the following functional dependence of h and d on D and V:

Table 2 Material property and parameters for the Johnson–Cook plasticity model for AISI 304L stainless steel

| ρ (kg/mm³)	E (MPa)	v	A (MPa)	B (MPa)	n	C	$\dot{\epsilon}_0 (s^{-1})$	m
7900	193,000	0.3	280	1597	0.25	0.097	1	2.044
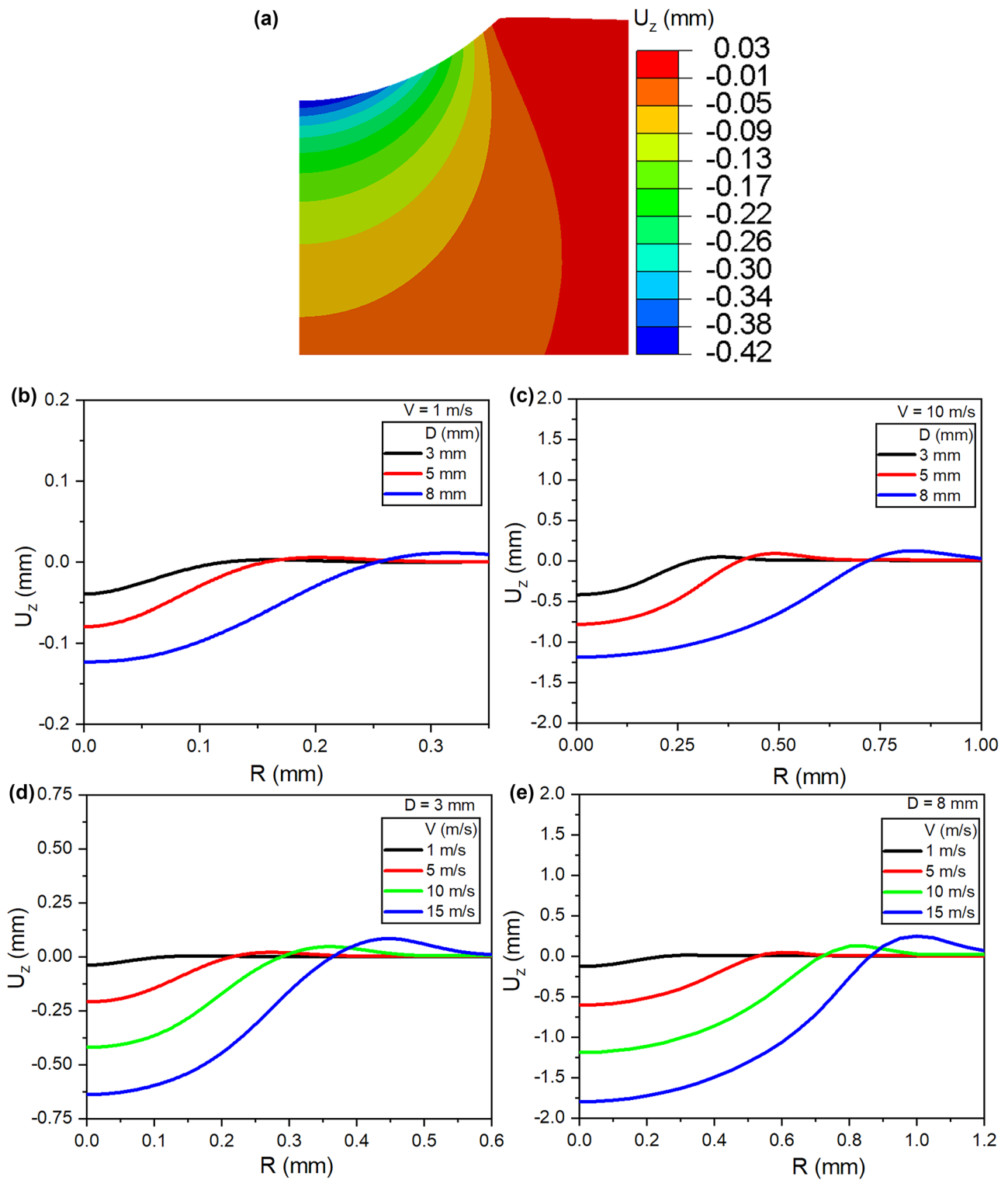
Fig. 8 a Contour plots of displacement, u_z, in SMATed material using shot size, $D = 3$ mm, and shot velocity, $V = 10$ m/s. **b** The variation of u_z of top surface along radial direction for material SMATed using different size of shot corresponding to **b** $V = 1$ m/s and **c** $V = 10$ m/s. The corresponding plots generated for the fixed shot size: **d** $D = 3$ mm and **e** $D = 8$ mm pertaining to different values of V

Fig. 9 The variation of **a** indent depth, h, and **b** indent diameter, d, in parametric space of V and D
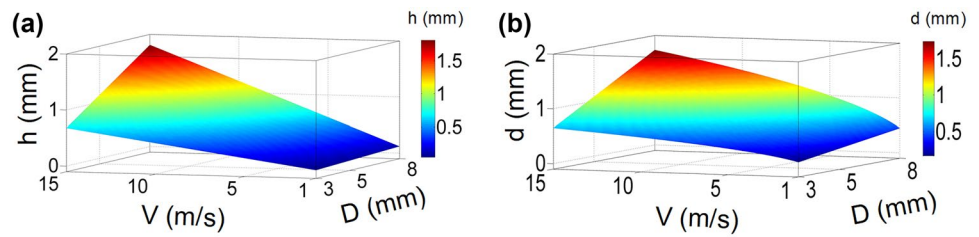
$$h = K_h DV, \tag{2}$$

$$d = K_d DV^{0.5}. \tag{3}$$

Here, K_h and K_d are experimentally obtained constants related to the hardness of the material. By fitting the empirical relations in Eqs. 2 and 3 on 3D surface plots shown in Fig. 9a, b, respectively, the values of K_h and K_d are determined to be 0.015 (s/m) and 0.055 (s/m)$^{0.5}$, respectively. A similar trend of d and h has also been reported in the literature [43]. Note that the parameters d and h can be linked to the surface roughness of SMATed material. Thus, using Eqs. 2 and 3, one can estimate the size and shape of the indent produced by SMAT using given parameters D and V.

4.2 Influence of parameters D and V on the residual strain in SMATed material

In Fig. 10a, the contour plots of equivalent plastic strain, $\bar{\epsilon}^p$, below the indent in a material SMATed using $D = 3$ mm and

$V = 10$ m/s are displayed in undeformed configuration. The region undergoing plastic deformation is almost circular, and $\bar{\epsilon}^p$ seems to be maximum near the top surface and drops with an increase in depth. Note, Zhou et al. [44] have also reported a qualitatively similar trend in the variation of $\bar{\epsilon}^p$ in AISI 301LN steel after single impact of a shot. To understand the effect of ball size on the distribution of $\bar{\epsilon}^p$ inside treated material, the variation of $\bar{\epsilon}^p$ along the z-axis for different values of D corresponding to $V = 1$ m/s is shown in Fig. 10b. Note from this figure that, for all values of D, $\bar{\epsilon}^p$ is maximum near the top surface and drops rapidly with an increase in z. It is important to note that the value of $\bar{\epsilon}^p$ near top surface changes marginally with an increase in ball size. It is also assumed that the material at a point has yielded if $\bar{\epsilon}^p$ exceed beyond 0.005, and the extent of the plastic zone along the depth (or plastic zone size) increases with an increase in D, as shown in Fig. 10b (refer inset diagram). The influence of V on the variation of $\bar{\epsilon}^p$ along depth is displayed in Fig. 10c for a fixed value of $D = 3$ mm. This figure shows a significant enhancement in the value of $\bar{\epsilon}^p$ at the free surface as well as inside the target material with an increase in V.

Fig. 10 **a** Contour plots of equivalent strain, $\bar{\epsilon}^p$, for shot size, $D = 3$ mm, and shot velocity, $V = 10$ m/s. The variation of $\bar{\epsilon}^p$ along the depth just below the center of impact in a SMATed material using **b** different values of D (having $V = 1$ m/s) and **c** different values of V (having $D = 3$ mm)
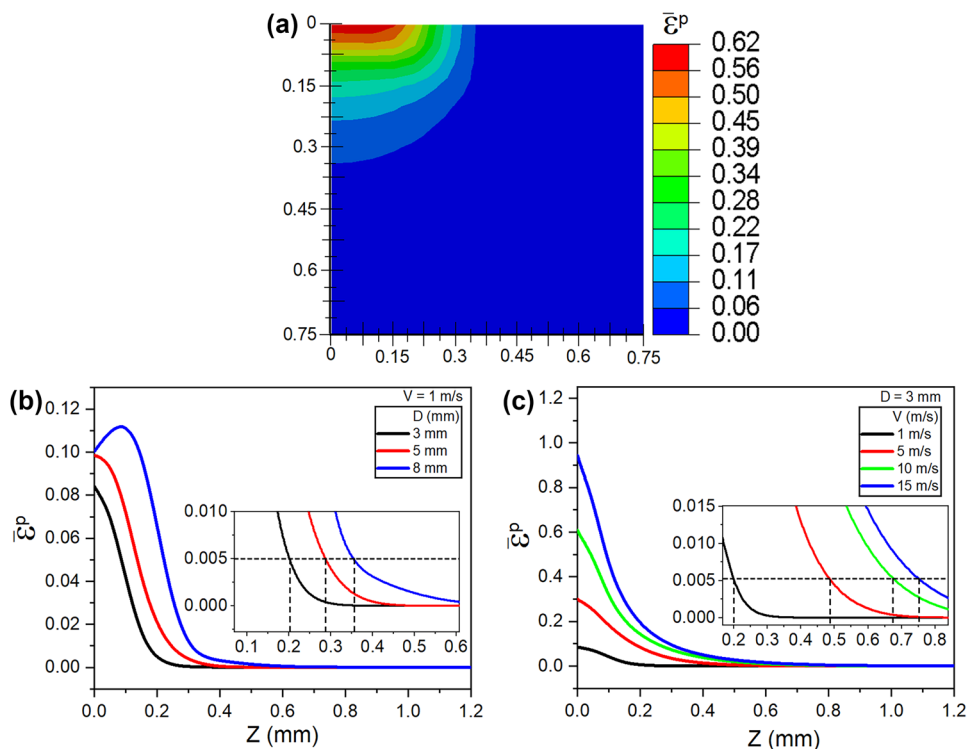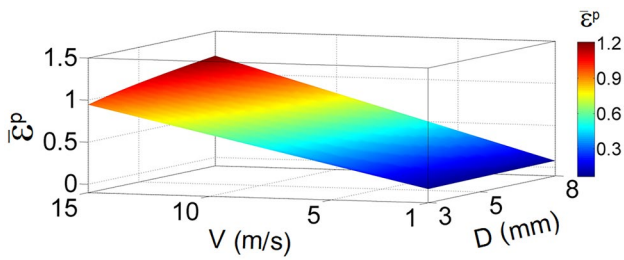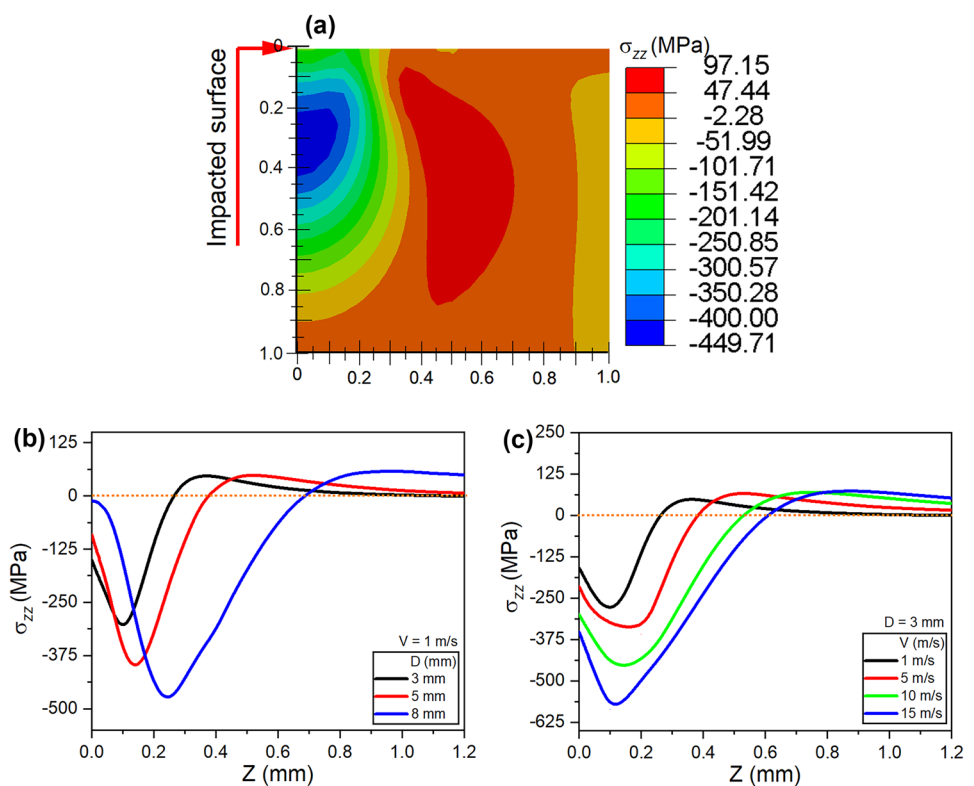
Fig. 11 Equivalent plastic strain, $\bar{\epsilon}^p$, measured at the sample surface against processing parameters, shot size (D), and shot velocity (V)

Considerable increase in the plastic zone size can also be perceived with enhancement in V. The variation of $\bar{\epsilon}^p$ at the top surface against D and V is shown in Fig. 11. It gives more insights into the effect of processing parameters on the development of plastic strain near the surface in a treated material. This figure confirms that *the residual strain near the top surface in SMATed material increases rapidly with an increase in impact velocity; however, it enhances marginally with increased ball diameter*. In other words, Figs. 10 and 11 suggest that *when the amount of plastic deformation near the free surface needs to be enhanced, one should increase the impact velocity. On the other hand, ball size should be increased when plastic zone size (or thickness of the treated layer) needs to be increased without changing plastic strain considerably at the free surface*.

Note that the twins and dislocations are fundamental carriers of plasticity in metals, and their intensity or volume fraction is correlated with the accumulated plastic strain. Since the residual plastic strain near the top surface is marginally influenced by D (see Fig. 11), the intensity or volume fraction of twins near the top surface is marginally affected by ball size in the experiments (refer Fig. 3b).

4.3 Influence of parameters D and V on the residual stress in SMATed material

Figure 12a displays the spatial distribution of the residual stress, σ_{zz}, in the undeformed configuration in a SMATed material using $D = 3$ mm and $V = 10$ m/s. It can be noticed that σ_{zz} is compressive in an elliptical region underneath the indent; however, it is tensile outside this region. Furthermore, σ_{zz} along the centerline, below the indent, increases with distance to attain its peak and begins to drop after that, suggesting that the location of maximum residual stress is not the surface of the SMATed target; instead, it is slightly below the surface. A similar trend in the distribution of residual stress has also been reported in the literature [8, 14, 45, 46]. Figure 12b displays the variation of σ_{zz} along the line $r = 0$ below the indent in a SMATed material for different values of D corresponding to $V = 1$ m/s. This figure confirms that, irrespective of ball diameter, the residual stress is compressive at the top surface, and its magnitude decreases
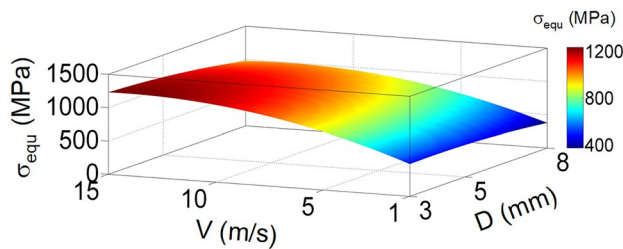
Fig. 12 a Contour plots of equivalent stress, σ_{zz}, for shot size, $D = 3$ mm, and shot velocity, $V = 10$ m/s. The variation of σ_{zz} along the depth just below the center of impact in the SMATed material using **b** different values of D (having $V = 1$ m/s) and **c** different values of V (having $D = 3$ mm)

Fig. 13 Residual equivalent stress, σ_{eq}, measured at the sample surface against processing parameters, shot size (D), and shot velocity (V)

with an increase in ball diameter. Furthermore, irrespective of ball size, the magnitude of σ_{zz} increases rapidly with an initial increase in depth to attain a maximum at some point below the top surface. This maximum value of compressive residual stress, the depth at which it is attained, enhances with an increase in D. As z increases further, the magnitude of σ_{zz} begins to drop, which leads to a changeover in its sign from compressive to tensile at a certain depth. Figure 12b also shows that *the thickness of material with compressive stress enhances with an increase in D.*

Figure 12c shows the effect of V on the variation of σ_{zz} below the indent for a fixed value of $D = 3$ mm. It can be seen that the magnitude of σ_{zz} at the surface and the maximum compressive stress inside the treated material increase with an increase in V. However, the depth corresponding to maximum stress enhances marginally with a rise in V. Thus, it can be concluded from Fig. 12 that *the value of maximum compressive residual stress can be enhanced by increasing either ball diameter or impact velocity, whereas the depth at which it is attained is mainly governed by ball diameter.*

Furthermore, the material thickness with compressive residual stress increases with an increase in V (as shown in Fig. 12c), akin to the trend noticed in Fig. 12b, implying that *the depth of material experiencing compressive residual stress can be controlled by both the parameters D and V.* The surface plot of Mises-equivalent stress, σ_{eq}, on the top

surface is displayed in Fig. 13 to get more insights on the effect of *D* and *V* on the residual stresses on the treated surface of the material. This figure clearly shows that *the residual equivalent stress at the top surface is mainly governed by impact velocity and poorly influenced by ball diameter.*

It has been seen in the above Sects. 4.1 to 4.3 that the processing parameters *D* and *V* have a marked effect on the indentation depth and size, plastic zone size, and distribution of residual stresses and strains. Since the deformation history influences the material's hardness, it is instructive to investigate these parameters' influence on a treated layer's hardness profile. Therefore, in the following section, the influence of *D* and *V* on the hardness variation below indent is computed through FE simulations of Berkovich indentation on material subjected to single impact. The residual strains and stresses determined in this section would be used as pre-strain and pre-stress in the calculations performed in the next section.

5 Computation of hardness in a SMATed material

5.1 Finite element simulation to generate hardness-depth profiles

In this section, the effect of parameters *D* and *V* on the variation of hardness along the SMATed layer is investigated by performing 2D axisymmetric finite element simulations of Berkovich indentation using a "Berkovich equivalent" conical-spherical rigid indenter (refer to Fig. 14b) [47, 48]. Figure 14a shows finite element discretization of SMATed target $(6000(L) \times 6000 \text{ nm}(H))$ using the four-noded axisymmetric element with reduced integration (CAX4R) along with rigid spherical indenter in the $r - z$ plane. The nodes lying on edges $r = 0$ and $z = 0$ are constrained to move along r and z directions, respectively; however, the indenter is assigned a prescribed displacement rate along the z direction. The coefficient of friction between indenter and surface is taken to be 0.2 [35]. Furthermore, the material is assumed to follow the rate-dependent Johnson–Cook

Fig. 14 **a** 2D axisymmetric finite element model employed in nanoindentation simulations using Berkovich-equivalent conical-spherical indenter. **b** Zoomed-in view of the mesh below the indenter. **c** Schematic displaying points considered below indent to record pre-stress and pre-strain from simulations of SMAT (performed in Sect. 4)
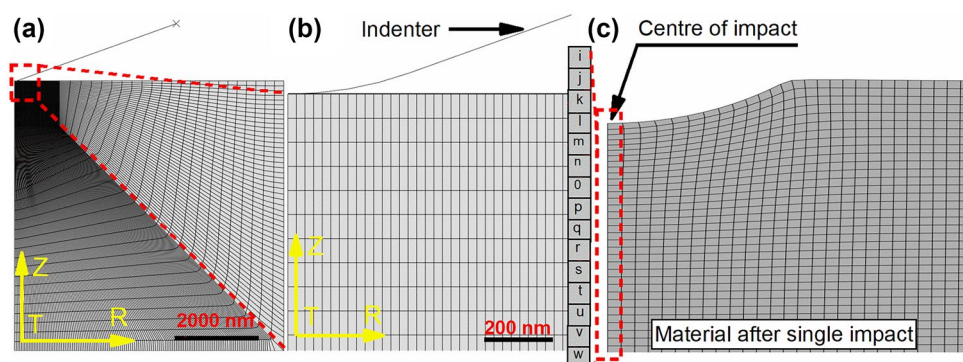
model (refer Eq. 1), and the material properties are taken identical to that mentioned in the previous section. Pre-stresses and pre-strains are also assigned to all the elements. As mentioned earlier, these nanoindentation simulations are aimed to compute the variation in hardness along the depth of a material SMATed using a particular set of parameters D and V. Therefore, to determine the hardness at a specific depth, z, in the material SMATed using particular process parameters, the equivalent plastic strain values, $\bar{\epsilon}^p$, and all the six components of residual stresses (σ_{ij}; i & $j = r, \theta$) are recorded from the simulations of single impact (performed using identical parameters in the previous section) and assigned them as pre-strains and pre-stresses to all elements in the present indentation simulations. Thus, the material in nanoindentation simulations resembles the material lying at a prescribed depth, z, in the SMATed material. For a given processing parameter, D and V, 15 equally spaced points (i–w) shown in Fig. 14c are taken in the SMATed material along the z-axis below the indent. The values of $\bar{\epsilon}^p$ and σ_{ij} at these points (obtained from the FE simulations, which are performed in

the previous section) are used as pre-strain and pre-stress in the nanoindentation simulations to determine hardness at different depths of z in a treated material. Thus, for a given D and V, 15 simulations of nanoindentation are performed to generate a hardness-depth profile of treated material. Hardness, H, is calculated using the well-known relation:

$$H = \frac{F_{max}}{A} \tag{4}$$

where, F_{max} is the maximum force obtained in the load–displacement curve after indentation and A is the area of the indent.

## 5.2 Influence of parameters D and V on the hardness of SMATed material

Figure 15a shows the variation of normalized hardness, H/H_o, along the depth, z, in a material SMATed using D = 3 and 8 mm, but a fixed value of V = 10 m/s. Here, H_o
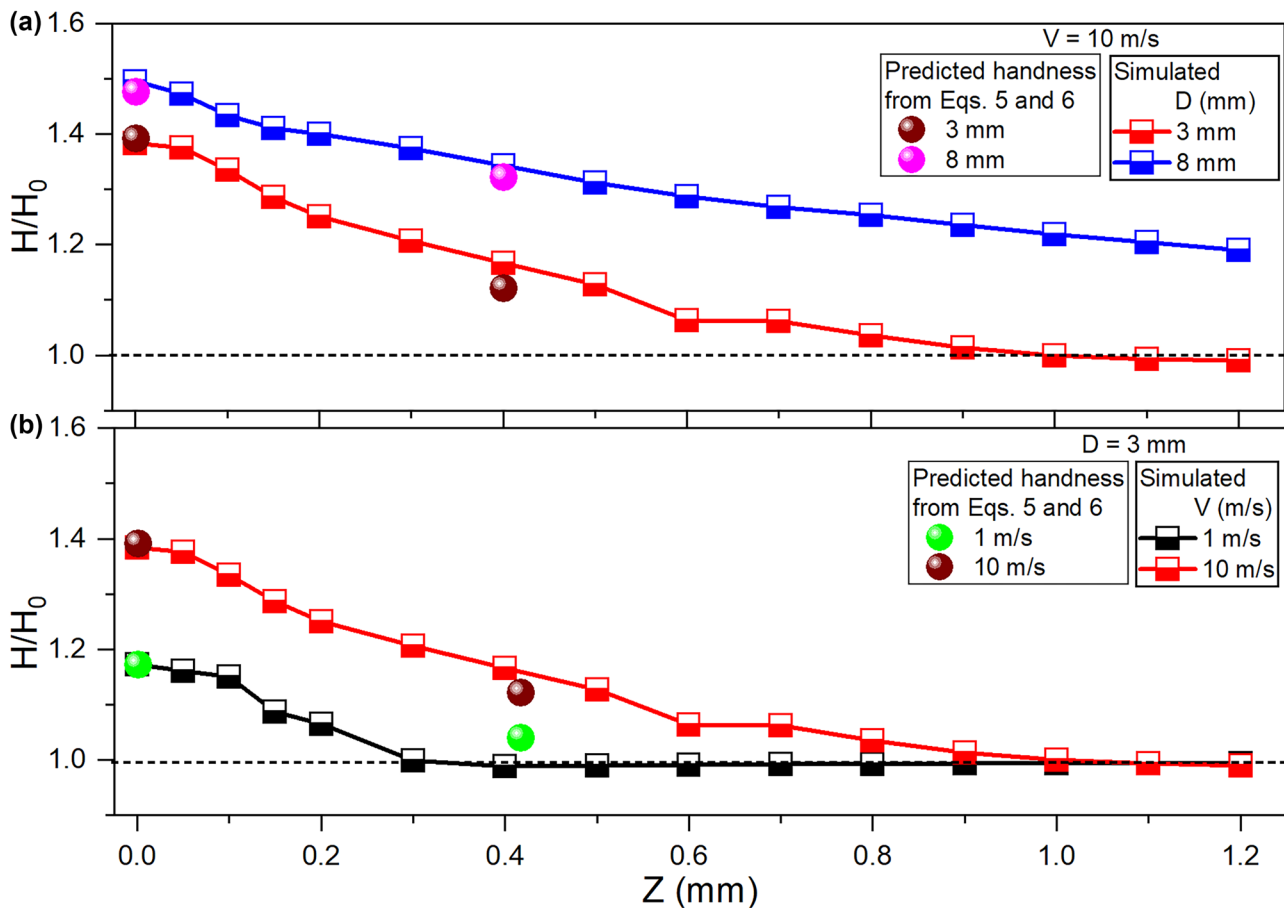
Fig. 15 The variation of hardness, H, normalized by initial hardness, H_0, of bare (non-SMATed) material along the depth in SMATed material for different values of **a** shot size, D, corresponding to shot velocity, V = 10 m/s, and **b** shot velocity, V, corresponding to D = 3 mm. The simulated hardness values are also compared with the hardness value, predicted from Eqs. 5 and 6

Fig. 16 Surface plots of normalized hardness, H/H_0, against velocity, V, and shot diameter, D, at **a** top surface and **b** depth of 400 μm of the SMATed material
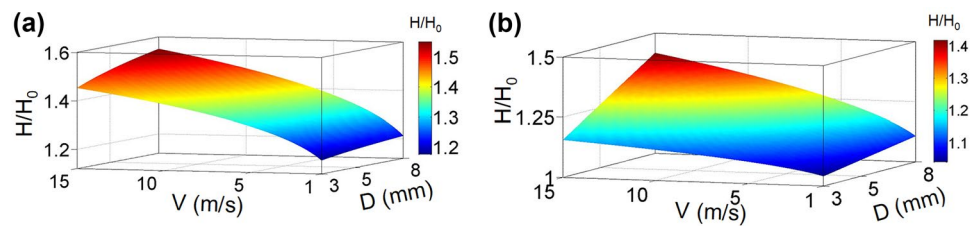
represents the initial hardness of the material (i.e., non-treated material). It can be seen from this figure that, irrespective of the D values, the hardness is maximum at the free surface, and it decreases with an increase in depth. Furthermore, the hardness values at the surface enhance marginally, while the thickness of the hardened layer (the value of z corresponding to $H/H_o=1$) increases significantly with an increase in D (see Fig. 15a). This observation is similar to that trend noticed in the experiments (refer to Fig. 5). Since equivalent stress and strain at the surface increases marginally, but the plastic zone size grows significantly, with an increase in D (refer Figs. 10a, 11, and 13), the hardness at the surface increases marginally, but the thickness of hardened layer enhances considerably with D in Fig. 15a. Figure 15b demonstrates the influence of impact velocity on the hardness profile in a SMATed material using a fixed ball size of 3 mm. It can be seen that H/H_o at the top surface increases by around 18% when V is increased from 1 to 10 m/s. Also, the hardened layer thickness is significantly increased from ~400 to 800–850 μm. This behavior is observed because the residual strain, stress at the surface, and plastic zone size increase with the increase in V, as noted in Figs. 10b, 11, and 13.

Values of H/H_o at $z = 0$ (surface) and 400 μm are plotted against D and V in Fig. 16a, b, respectively, to get more insights on the processing parameters' influence on the hardness variation along the depth of SMATed material. Figure 16a shows that, at the top surface, H/H_o enhances significantly with an increase in V (for a fixed D value); however, it increases marginally with D (irrespective of V). By comparing Fig. 5b, c with Fig. 15a, it can be noticed that the present FE simulations predict qualitatively similar dependence of surface hardness on the processing parameters as observed from experiments, although differences of 10–17% in the values of H/H_o can be noticed. Furthermore, Fig. 16b shows that the hardness at a depth of 400 μm increases with D for all V values, but enhancement is more pronounced for higher V. Also, H/H_o enhances more strongly with an increase in V for larger D (see Fig. 16b). *Thus, it can be concluded that hardness at the surface of the treated material is mainly governed by the impact velocity and poorly influenced by ball diameter. However, hardness away from the surface is influenced by both the ball diameter and impact velocity.* Furthermore, the following

empirical relations showing the functional dependence of H/H_o on the parameters D and V are determined by fitting 3D plots displayed in Fig. 16a, b for $z = 0$ and 400 μm, respectively:

$$\frac{H}{H_o} = 1 + C_0 D^{0.2} V^{0.35} \tag{5}$$

$$\frac{H}{H_o} = 1 + C_{400} D V^{0.5} \tag{6}$$

Here, the parameters C_0 and C_{400} are fitting constants for $z = 0$ and 400 μm, respectively, and these are found to be 0.14 $(s/m)^{0.35}$ and 0.013 $(s/m)^{0.5}$, respectively. The above relations provide an estimate of hardness value at the top surface and a depth of ~400 μm in a SMATed material for given values of processing parameters D and V. Equations 5 and 6 provide guidelines in choosing an appropriate combination of process parameters D and V to achieve the desired hardness at the surface and inside the treated layer in SMATed material, respectively. In other words, one can estimate the values of D and V beforehand using Eqs. 5 and 6 to achieve desired hardness at the surface or inside the layer through SMAT process. Thus, the number of experiments and, hence, the associated cost can be minimized to achieve the required hardness.

6 Conclusions

In this work, the surface mechanical attrition treatment (SMAT) process is carried out on AISI 304L steel using 3- and 8-mm diameter balls of high-carbon steel (AISI 52,100/EN31) with impact velocities of 1 (± 0.2) and 10 (± 1.2) m/s. The hardness variation along the SMATed layer's depth is determined through nanoindentation. The complementary finite element (FE) simulations of the single impact SMAT process using the rate-dependent Johnson–Cook plasticity model are performed to provide the mechanistic reasons for trends in hardness variation observed from the experiments. A strategy to compute the hardness-depth profile of SMATed material through finite element simulations is also developed. The important conclusions from the present work are as follows:

- The SEM micrographs of the cross-section of SMATed material show that the twin distribution near top surface changeover from coarser to finer when impact velocity, V, is increased from a low to significantly high value; however, it changes marginally with an increase in ball diameter, D.
- Nanoindentation experiments performed along the depth of SMATed material reveal that the hardness near-surface is mainly governed by V and weakly influenced by D. However, the hardened layer thickness can be enhanced by increasing either of these parameters.
- The FE simulations of the single impact SMAT process show significant enhancement in the pile-up around the impression with an increase in either D or V, which suggests that the treated surface roughness would increase with an increase in D and V.
- The FE analysis shows that the residual equivalent plastic strain, $\bar{\epsilon}^p$, and Mises equivalent stress, σ_{eq}, near the top surface are mainly controlled by V and poorly influenced by D.
- The FE simulations of nanoindentation on SMATed material's cross-section show that the surface hardness is mainly controlled by V and marginally influenced by D. This behavior is explained by noting the effects of D and V on the residual equivalent stress and equivalent plastic strain at the surface. However, the hardness away from the surface is influenced by both parameters (i.e., shot size and shot velocity).
- The empirical relation between hardness at the surface (and the depth of ~ 400 μm) and processing parameters (D and V) is determined through FE simulations.

The present work provides a guideline in selecting suitable values of ball diameter and impact velocity to achieve the desired surface properties such as hardness and thickness of the hardened layer through the SMAT process.

Declarations

Ethics approval This research does not involve human participants and/or animals.

Consent to participate All authors have read and approved the final manuscript.

Consent for publication All authors have read and agreed to publish the final version of the manuscript.

Competing interests The authors declare no competing interests.

References

1. Kheiri S, Mirzadeh H, Naghizadeh M (2019) Tailoring the microstructure and mechanical properties of AISI 316L austenitic stainless steel via cold rolling and reversion annealing. Mater Sci Eng, A 759:90–96. https://doi.org/10.1016/j.msea.2019.05.028
2. San Marchi C, Ronevich JA, Sabisch JEC, Sugar JD, Medlin DL, Somerday B (2020) Effect of microstructural and environmental variables on ductility of austenitic stainless steels. Int J Hydrogen Energy 46(23):12338–12347. https://doi.org/10.1016/j.ijhydene.2020.09.069
3. Capeletti T, Louthan M Jr (1977) The tensile ductility of austenitic steels in air and hydrogen. J Eng Mater Technol 99(2):153–158. https://doi.org/10.1115/1.3443426
4. Hosseinalipour S, Ershad-Langroudi A, Hayati AN, Nabizade-Haghighi A (2010) Characterization of sol–gel coated 316L stainless steel for biomedical applications. Prog Org Coat 67(4):371–374. https://doi.org/10.1016/j.porgcoat.2010.01.002
5. Rho BS, Hong HU, Nam SW (2000) The effect of δ-ferrite on fatigue cracks in 304L steels. Int J Fatigue 22(8):683–690. https://doi.org/10.1016/S0142-1123(00)00043-8
6. Soyama H (2020) Comparison between shot peening, cavitation peening, and laser peening by observation of crack initiation and crack growth in stainless steel. Metals 10(1):63. https://doi.org/10.3390/met10010063
7. Tian J, Villegas J, Yuan W, Fielden D, Shaw L, Liaw P, Klarstrom D (2007) A study of the effect of nanostructured surface layers on the fatigue behaviors of a C-2000 superalloy. Mater Sci Eng, A 468:164–170. https://doi.org/10.1016/j.msea.2006.10.150
8. Wang C, Wang C, Wang L, Lai Y, Li K, Zhou Y (2020) A dislocation density–based comparative study of grain refinement, residual stresses, and surface roughness induced by shot peening and surface mechanical attrition treatment. The International Journal of Advanced Manufacturing Technology 108:505–525. https://doi.org/10.1007/s00170-020-05413-8
9. Ke L, Jian L (1999) Surface nanocrystallization (SNC) of metallic materials-presentation of the concept behind a new approach. J Mater Sci Technol 15(3):193–197. https://www.scopus.com/record/display.uri?eid=2-s2.0-0000506802&origin=recordpage. Accessed 3 Mar 2021
10. Gatey A, Hosmani S, Singh R (2016) Surface mechanical attrition treated AISI 304L steel: role of process parameters. Surf Eng 32(1):69–78. https://doi.org/10.1179/1743294415Y.0000000056
11. Zhu L, Guan Y, Wang Y, Xie Z, Lin J (2017) Influence of process parameters of ultrasonic shot peening on surface nanocrystallization and hardness of pure titanium. Int J Adv Manuf Technol 89(5–8):1451–1468. https://doi.org/10.1007/s00170-016-9181-4

12. Lin Y, Cai Z-B, Li Z-Y, Yin M-G, Wang W-J, He W-F, Zhou Z-R (2019) Study on the abrasive wear behavior of laser shock peening Ti-6Al-4V titanium alloy under controlled cycling impact. Wear 426:112–121. https://doi.org/10.1016/j.wear.2019.01.112

13. Goli F, Jamaati R (2019) Effect of strain path during cold rolling on the microstructure, texture, and mechanical properties of AA2024 aluminum alloy. Materials Research Express 6(6):066514. https://doi.org/10.1088/2053-1591/ab0a1f

14. Astaraee AH, Miresmaeili R, Bagherifard S, Guagliano M, Aliofkhazraei M (2017) Incorporating the principles of shot peening for a better understanding of surface mechanical attrition treatment (SMAT) by simulations and experiments. Mater Des 116:365–373. https://doi.org/10.1016/j.matdes.2016.12.045

15. Wen M, Wen C, Hodgson P, Li Y (2012) Thermal oxidation behaviour of bulk titanium with nanocrystalline surface layer. Corros Sci 59:352–359. https://doi.org/10.1016/j.corsci.2012.03.005

16. Wang L, Wang Z, Lu K (2011) Grain size effects on the austenitization process in a nanostructured ferritic steel. Acta Mater 59(9):3710–3719. https://doi.org/10.1016/j.actamat.2011.03.006

17. Frontán J, Zhang Y, Dao M, Lu J, Gálvez F, Jérusalem A (2012) Ballistic performance of nanocrystalline and nanotwinned ultrafine crystal steel. Acta Mater 60(3):1353–1367. https://doi.org/10.1016/j.actamat.2011.11.029

18. Bahl S, Shreyas P, Trishul M, Suwas S, Chatterjee K (2015) Enhancing the mechanical and biological performance of a metallic biomaterial for orthopedic applications through changes in the surface oxide layer by nanocrystalline surface modification. Nanoscale 7(17):7704–7716. https://doi.org/10.1039/C5NR00574D

19. Olugbade TO, Lu J (2020) Literature review on the mechanical properties of materials after surface mechanical attrition treatment (SMAT). Nano Materials Science 2(1):3–31. https://doi.org/10.1016/j.nanoms.2020.04.002

20. Dureau C, Novelli M, Arzaghi M, Massion R, Bocher P, Nadot Y, Grosdidier T (2020) On the influence of ultrasonic surface mechanical attrition treatment (SMAT) on the fatigue behavior of the 304L austenitic stainless steel. Metals 10(1):100. https://doi.org/10.3390/met10010100

21. Chan H, Ruan H, Chen A, Lu J (2010) Optimization of the strain rate to achieve exceptional mechanical properties of 304 stainless steel using high speed ultrasonic surface mechanical attrition treatment. Acta Mater 58(15):5086–5096. https://doi.org/10.1016/j.actamat.2010.05.044

22. Tao N, Wang Z, Tong W, Sui M, Lu J, Lu K (2002) An investigation of surface nanocrystallization mechanism in Fe induced by surface mechanical attrition treatment. Acta Mater 50(18):4603–4616. https://doi.org/10.1016/S1359-6454(02)00310-5

23. Zhang X, Lu J, Shi S (2011) A computational study of plastic deformation in AISI 304 induced by surface mechanical attrition treatment. Mech Adv Mater Struct 18(8):572–577. https://doi.org/10.1080/15376494.2011.621828.

24. Tao N, Zhang H, Lu J, Lu K (2003) Development of nanostructures in metallic materials with low stacking fault energies during surface mechanical attrition treatment (SMAT). Mater Trans 44(10):1919–1925. https://doi.org/10.2320/matertrans.44.1919

25. Arifvianto B, Mahardika M, Dewo P, Iswanto P, Salim U (2011) Effect of surface mechanical attrition treatment (SMAT) on microhardness, surface roughness and wettability of AISI 316L. Mater Chem Phys 125(3):418–426. https://doi.org/10.1016/j.matchemphys.2010.10.038

26. Samih Y, Beausir B, Bolle B, Grosdidier T (2013) In-depth quantitative analysis of the microstructures produced by Surface Mechanical Attrition Treatment (SMAT). Mater Charact 83:129–138. https://doi.org/10.1016/j.matchar.2013.06.006

27. Novelli M, Bocher P, Grosdidier T (2018) Effect of cryogenic temperatures and processing parameters on gradient-structure of a stainless steel treated by ultrasonic surface mechanical attrition treatment. Mater Charact 139:197–207. https://doi.org/10.1016/j.matchar.2018.02.028

28. Edberg J, Lindgren LE, Ken-Ichiro M (1995) Shot peening simulated by two different finite element formulations. International Conference on Numerical Methods in Industrial Forming Processes: Balkema Publishers, AA/Taylor & Francis The Netherlands, 18/06/1995–21/06/1995

29. Guagliano M (2001) Relating Almen intensity to residual stresses induced by shot peening: a numerical approach. J Mater Process Technol 110(3):277–286. https://doi.org/10.1016/S0924-0136(00)00893-1

30. Chen Z, Sun Z, Panicaud B (2018) Constitutive modeling of TWIP/TRIP steels and numerical simulation of single impact during Surface Mechanical Attrition Treatment. Mech Mater 122:69–75. https://doi.org/10.1016/j.mechmat.2018.04.005

31. Herrera C, Ponge D, Raabe D (2011) Design of a novel Mn-based 1 GPa duplex stainless TRIP steel with 60% ductility by a reduction of austenite stability. Acta Mater 59(11):4653–4664. https://doi.org/10.1016/j.actamat.2011.04.011

32. Mahato B, Sahu T, Shee S, Sahu P, Sawaguchi T, Kömi J, Karjalainen L (2017) Simultaneous twinning nucleation mechanisms in an Fe–Mn–Si–Al twinning induced plasticity steel. Acta Mater 132:264–275. https://doi.org/10.1016/j.actamat.2017.04.046

33. Abreu HF, Carvalho SS, Lima Neto PD, Santos RP, Freire VN, Silva PM, Tavares SS (2007) Deformation induced martensite in an AISI 301LN stainless steel: characterization and influence on pitting corrosion resistance. Mater Res 10(4):359–366. https://doi.org/10.1590/S1516-14392007000400007

34. Tiamiyu A, Szpunar J, Odeshi A (2019) Strain rate sensitivity and activation volume of AISI 321 stainless steel under dynamic impact loading: grain size effect. Mater Charact 154:7–19. https://doi.org/10.1016/j.matchar.2019.05.027

35. Miao HY, Larose S, Perron C, Lévesque M (2009) On the potential applications of a 3D random finite element model for the simulation of shot peening. Adv Eng Softw 40(10):1023–1038. https://doi.org/10.1016/j.advengsoft.2009.03.013

36. Johnson GR, Cook WH (1985) Fracture characteristics of three metals subjected to various strains, strain rates, temperatures and pressures. Eng Fract Mech 21(1):31–48. https://doi.org/10.1016/0013-7944(85)90052-9

37. Wu G, Wang Z, Gan J, Yang Y, Meng Q, Wei S, Huang H (2019) FE analysis of shot-peening-induced residual stresses of AISI 304 stainless steel by considering mesh density and friction coefficient. Surf Eng 35(3):242–254. https://doi.org/10.1080/02670844.2018.1470817

38. Cai S, Liu J, Zhang P, Li C, Cheng Y (2020) Dynamic response of sandwich panels with multi-layered aluminum foam/UHMWPE laminate cores under air blast loading. Int J Impact Eng 138:103475. https://doi.org/10.1016/j.ijimpeng.2019.103475

39. Maurel-Pantel A, Fontaine M, Thibaud S, Gelin J-C (2012) 3D FEM simulations of shoulder milling operations on a 304L stainless steel. Simul Model Pract Theory 22:13–27. https://doi.org/10.1016/j.simpat.2011.10.009

40. Tasdemirci A, Sahin S, Kara A, Turan K (2015) Crushing and energy absorption characteristics of combined geometry shells at quasi-static and dynamic strain rates: experimental and numerical study. Thin-Walled Structures 86:83–93. https://doi.org/10.1016/j.tws.2014.09.020

41. Singh D, Basha DA, Singh A, Devan RS, Hosmani SS (2020) Microstructural and passivation response of severely deformed AISI 304 steel surface: the role of surface mechanical attrition

treatment. J Mater Eng Perform 29(10):6898–6911. https://doi.org/10.1007/s11665-020-05161-6

42. Iida K (2000) Dent and affected layer produced by shot peening. The Shot Peener 14(3):4-7

43. Ghelichi R, Crispiatico G, Guagliano M, Bagherifard S (2018) An energetic approach to predict the effect of shot peening-based surface treatments. Metals 8(3):190. https://doi.org/10.3390/met8030190

44. Zhou F, Jiang W, Du Y, Xiao C (2019) A comprehensive numerical approach for analyzing the residual stresses in AISI 301LN stainless steel induced by shot peening. Materials 12(20):3338. https://doi.org/10.3390/ma12203338

45. Meguid S, Shagal G, Stranart J (2002) 3D FE analysis of peening of strain-rate sensitive materials using multiple impingement model. Int J Impact Eng 27(2):119–134. https://doi.org/10.1016/S0734-743X(01)00043-4

46. Jianming W, Feihong L, Feng Y, Gang Z (2011) Shot peening simulation based on SPH method. Int J Adv Manuf Technol 56(5–8):571–578. https://doi.org/10.1007/s00170-011-3193-x

47. Hirmukhe S, Prasad KE, Singh I (2020) Investigation of pressure sensitive plastic flow in nanoglasses from finite element simulations. Scripta Mater 180:45–50. https://doi.org/10.1016/j.scriptamat.2020.01.022

48. Lichinchi M, Lenardi C, Haupt J, Vitali R (1998) Simulation of Berkovich nanoindentation experiments on thin films using finite element method. Thin Solid Films 312(1–2):240–248. https://doi.org/10.1016/S0040-6090(97)00739-6